

Biogenic gas nanostructures as ultrasonic molecular reporters

Mikhail G. Shapiro^{1,2,3†*}, Patrick W. Goodwill², Arkosnato Neogy⁴, Melissa Yin⁵, F. Stuart Foster^{5,6}, David V. Schaffer^{2,7} and Steven M. Connelly^{2,4}

Ultrasound is among the most widely used non-invasive imaging modalities in biomedicine¹, but plays a surprisingly small role in molecular imaging due to a lack of suitable molecular reporters on the nanoscale. Here, we introduce a new class of reporters for ultrasound based on genetically encoded gas nanostructures from microorganisms, including bacteria and archaea. Gas vesicles are gas-filled protein-shelled compartments with typical widths of 45–250 nm and lengths of 100–600 nm that exclude water and are permeable to gas^{2,3}. We show that gas vesicles produce stable ultrasound contrast that is readily detected *in vitro* and *in vivo*, that their genetically encoded physical properties enable multiple modes of imaging, and that contrast enhancement through aggregation permits their use as molecular biosensors.

Contrast-enhanced ultrasound has been an active area of research and development for over 40 years⁴, with conventional ultrasound contrast agents formulated as lipid- or protein-stabilized gas microbubbles. The partial pressure gradient between a microbubble's gas interior and the surrounding media, which is inversely proportional to its radius, limits most microbubbles to sizes larger than 1 μm and leads to gas escape, bubble fragmentation and collapse after *in vivo* administration^{5,6}. Although microbubbles have been very successful in clinical imaging of the blood pool and related physiology⁷ and have recently been proposed as potential cell-internalized labels⁸, several factors limit their range of applications in molecular imaging. For example, microbubbles of micrometre size are typically limited to imaging targets within the vasculature. In addition, microbubbles typically have a short half-life compared to the *in vivo* dynamics of immune, stem and other cells^{5,7,9}. Furthermore, none of the solid¹⁰, liquid¹¹, hollow¹² or phase-change¹³ contrast agents proposed as microbubble alternatives have so far become widely adopted due to limitations in echogenicity, stability or ease of synthesis. As a result, important studies in oncology, immunology, regenerative medicine and other biomedical areas remain dominated by nanoparticle reporters designed for optical, magnetic resonance and nuclear imaging¹⁴.

We hypothesized that nanoscale reporters with novel properties for molecular ultrasonography could be derived from natural biological structures. In particular, we considered gas vesicles, genetically encoded gas nanostructures formed by certain bacteria and archaea as a means to control buoyancy for optimal access to light and nutrients^{2,3}. Gas vesicles have cylindrical or biconical shapes, with maximal diameters of 45–250 nm and typical lengths of 100–600 nm, varying between genetic hosts^{2,3}. These nanostructures

interact with gases through a mechanism that is fundamentally different from that in microbubbles. Whereas microbubbles trap pre-loaded gas, gas vesicles exclude water but permit gas from the surrounding media to freely diffuse in and out of their 1–10 nm interior through a 2 nm protein shell² (Fig. 1a). As a result, no pressure gradient exists between the inside and outside of gas vesicles, permitting them to be inherently stable despite their nanometre size. Although they were discovered over 100 years ago¹⁵ and have been well-characterized biophysically², gas vesicles have yet to be substantially exploited as a nanotechnology³. We hypothesized that such gas vesicles could serve as nanoscale molecular reporters for ultrasound imaging and, furthermore, that their genetically encoded structural properties, such as collapse at specific hydrostatic pressures, could enable new imaging modes beyond those available with microbubbles.

To test this hypothesis, gas vesicles from *Anabaena flos-aquae* (*Ana*) and *Halobacterium NRC-1* (*Halo*) (Fig. 1b,c), representing two genetically distant sources³, were purified through tonic cell lysis and centrifugally assisted flotation, and imaged in gel phantoms using a scanning single-element ultrasound imaging system operating at 4.8, 8.6 and 17 MHz (for sample preparation and imaging details, see Methods). Gas vesicles from both species produced robust contrast relative to buffer controls at optical densities (OD) ranging from 0.25 to 2.0 (Fig. 1d–g), corresponding to nanostructure concentrations of 150 pM to 1.2 nM (*Ana*) or 5 pM to 40 pM (*Halo*) and gas volume fractions of ~0.01–0.1%. Gas vesicle echogenicity in this configuration was detectable for over one week (Supplementary Fig. 1). Contrast was strongest at the highest frequency, with OD 2.0 *Ana* gas vesicles producing 27.0 ± 4.1 greater scattering than buffer controls (Fig. 1f). The balance of scattering and attenuation differed between *Ana* and *Halo* gas vesicles. Whereas *Ana* gas vesicles produced backscatter fairly uniformly along the axial dimension (from top to bottom in Fig. 1d), *Halo* gas vesicles at higher concentrations produced acoustic attenuation, manifested as a reduced signal beneath the vesicles in the gel phantom (Fig. 1e, Supplementary Fig. 2).

Gas vesicles can be collapsed by rapidly increasing the hydrostatic pressure past a species-specific critical point, ranging from 40 kPa to over 700 kPa (refs 2,16) (Fig. 1b,c). Gas vesicles that were hydrostatically collapsed before loading into the phantom failed to show ultrasound contrast, confirming the echogenic role of their gas compartments (Fig. 1d,e).

Nonlinear imaging modes relying on harmonic signals have been used to improve the contrast specificity of microbubble-enhanced

¹Miller Research Institute, University of California at Berkeley, 2536 Channing Way, Berkeley, California 94720, USA, ²Department of Bioengineering, 306 Stanley Hall MC #1762, University of California at Berkeley, Berkeley, California 94720, USA, ³Department of Molecular and Cell Biology, 142 LSA #3200, University of California at Berkeley, Berkeley, California 94720, USA, ⁴Department of Electrical Engineering and Computer Science, University of California at Berkeley, Berkeley, California 94720, USA, ⁵Sunnybrook Research Institute, University of Toronto, 2075 Bayview Avenue, Toronto, Ontario M4N 3M5, Canada, ⁶Department of Medical Biophysics, University of Toronto, 610 University Avenue, Toronto, Ontario M4N 3M5, Canada, ⁷Department of Chemical and Biomolecular Engineering, University of California at Berkeley, Berkeley, California 94720, USA. [†]Present address: Division of Chemistry and Chemical Engineering, California Institute of Technology, 1200 East California Boulevard, Pasadena, California 91125, USA. *e-mail: mikhail@caltech.edu

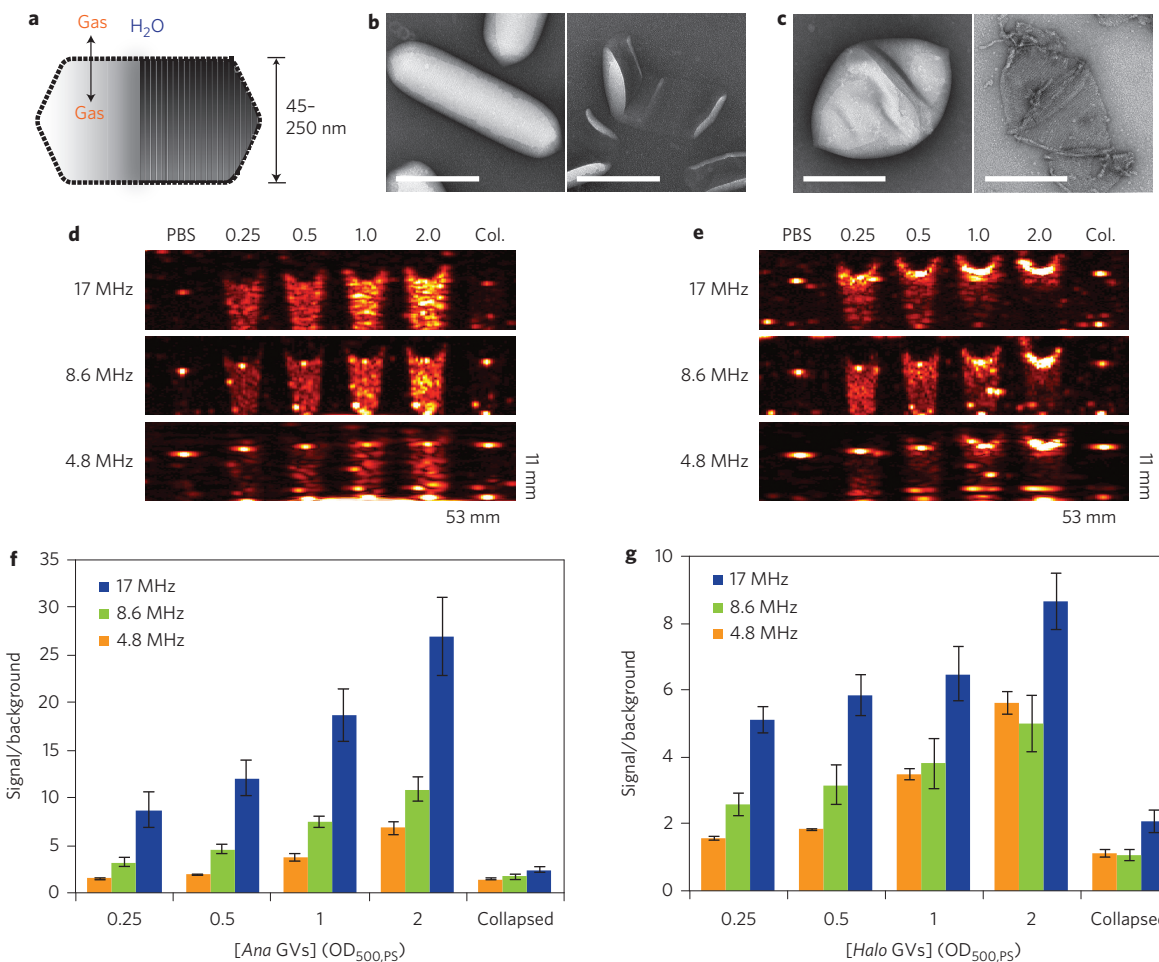


Figure 1 | Gas vesicles produce ultrasound contrast. **a**, Diagram of a gas vesicle: a hollow gas nanocompartment (solid shading) surrounded by a gas-permeable protein shell (ribbed shading). **b**, TEM images of intact (left) and hydrostatically collapsed (right) *Ana* gas vesicles. **c**, TEM images of intact (left) and collapsed (right) *Halo* gas vesicles. All scale bars, 200 nm. **d**, Ultrasound images of a gel phantom containing PBS buffer, *Ana* gas vesicles at optical densities ranging from OD 0.25 to 2 (concentrations of 150 pM to 1.2 nM) or collapsed *Ana* gas vesicles (OD 2.0). Images were acquired at multiple frequencies, as indicated. **e**, Ultrasound images of a gel phantom containing PBS buffer, *Halo* gas vesicles at optical densities ranging from OD 0.25 to 2 (concentrations of 5 to 40 pM) or collapsed *Halo* gas vesicles (OD 2.0). Conversion between OD, molar concentration and gas volume fraction is described in the Methods. The size of each field of view is indicated in the lower right corner of the images. **f**, Total backscattered signal relative to PBS at each frequency and *Ana* gas vesicle (GV) concentration ($N = 4$ per sample). **g**, Total backscattered signal relative to PBS at each frequency and *Halo* gas vesicle concentration ($N = 4$ per sample). Detailed image acquisition and analysis parameters are provided in Supplementary Table 1, and colour maps for ultrasound images in Supplementary Fig. 9. All error bars represent \pm standard error of the mean (s.e.m.).

ultrasound¹⁷. In particular, harmonic backscatter is thought to arise from oscillations in microbubble radius¹⁸ in response to incident pressure waves. We tested whether harmonics could also be detected from gas vesicles. Transmitting at 6 MHz, we observed substantial second- and third-harmonic signals in *Halo* gas vesicles at 12 MHz and 18 MHz compared to polystyrene microspheres, a linear scattering reference material (Fig. 2a). *Ana* gas vesicles did not produce harmonic signals at 6 MHz (Supplementary Fig. 3). Images formed by processing *Halo* gas vesicle signals through bandpass filters centred at the second and third harmonics showed 3.7-fold and 4.6-fold greater contrast enhancement in vesicle-containing wells relative to the linear scatterer than did images processed at the transmitted frequency (Fig. 2b,c). To further explore gas vesicle-specific contrast enhancement, we took advantage of pressure-induced vesicle collapse by testing its application *in situ* at ultrasound frequencies. *Halo* and *Ana* gas vesicles were imaged before and after a disruptive scan at 8.6 MHz in which the transducer output was set to produce a peak pressure of 650 kPa—above the critical collapse level of both species of vesicles (70–150 kPa for *Halo* and 440–605 kPa for *Ana*)¹⁶ (Fig. 2d). The gas vesicle signal was mostly eliminated,

enabling the generation of subtraction images in which the signal from *Halo* and *Ana* gas vesicle wells relative to polystyrene was boosted by factors of 10 and 22, respectively (Fig. 2d,e). Such subtraction images can be used to increase the specificity of contrast information relative to background scattering¹⁹.

The fact that gas vesicles from different species have distinct critical collapse pressures¹⁶ raised the further prospect of distinguishing multiple populations of vesicles in the same sample through ‘serial collapse’ imaging. In this paradigm, contrast originating from gas vesicles with a low collapse pressure is identified by its disappearance upon the application of pressure pulses with amplitudes above their critical point but below that of other vesicles. The remaining contrast is attributable to gas vesicle species with higher collapse pressures. To test this paradigm with our two species of vesicles, we prepared imaging phantoms with wells containing *Halo* gas vesicles, *Ana* gas vesicles, or a combination of both (Fig. 2f). In an initial image, both populations of vesicle produce contrast (Fig. 2f, top), but after low-pressure collapse at 300 kPa, contrast in the *Halo* gas vesicle well is eliminated and contrast in the mixed well is reduced (Fig. 2f, middle). After high-pressure collapse at 650 kPa, contrast in the

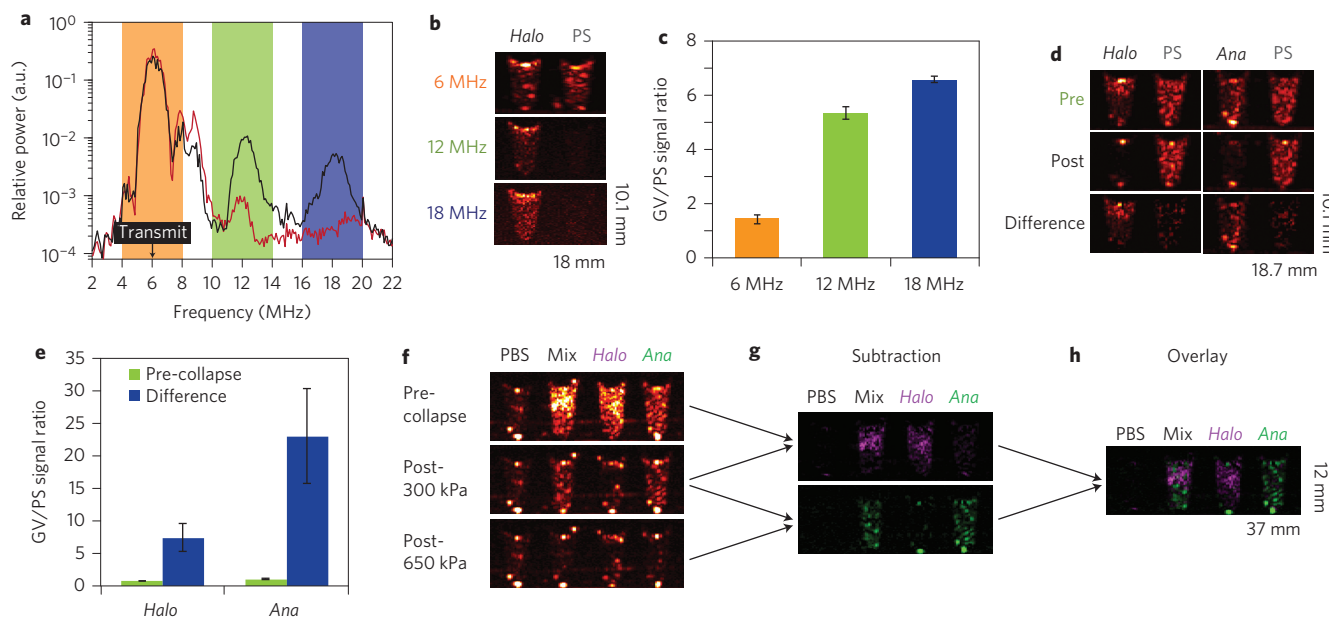


Figure 2 | Nonlinear imaging and genetic diversity enable enhanced contrast specificity and selective disruption imaging. **a**, Power spectrum of signal backscattered from *Halo* gas vesicles (black) and 4.78 μm polystyrene (PS) microspheres (red) in response to 6 MHz transmitted pulses (peak amplitude 98 kPa, labelled ‘Transmit’ in the figure). Each point on the spectrum represents an average of 48 points from three samples (16 points per sample). The orange, green and blue shaded areas correspond to frequency bands used to generate the images in **b**. **b**, Ultrasound images of *Halo* gas vesicles and PS microspheres acquired with 6 MHz transmission and bandpass-filtered around 6, 12 and 18 MHz. **c**, Ratio of total backscattered signal from *Halo* gas vesicles and PS microspheres after filtering at the indicated frequencies ($N = 4$). **d**, Ultrasound images of *Halo* gas vesicles, *Ana* gas vesicles and PS microspheres at 8.6 MHz acquired before (Pre) and after (Post) destructive collapse with 650 kPa insonation, and the difference (Difference) between these images. **e**, Ratio of total backscattered signal from gas vesicles and PS microspheres in pre-collapse and difference images ($N = 4$). The concentrations used in **a–e** were OD 0.5 *Halo* gas vesicles, OD 2.0 *Ana* gas vesicles and 0.83% (wt/vol) polystyrene. **f**, Ultrasound images of a phantom containing wells with PBS, a mixture of *Ana* and *Halo* gas vesicles, or each type of gas vesicle on its own (all gas vesicles at OD 1.0 in PBS), acquired at 8.6 MHz. Top: before collapse. Middle: after collapse at 300 kPa. Bottom: after collapse at 650 kPa. **g**, Top: Difference between the top and middle images in **f**. Bottom: Difference between the middle and bottom images in **f**. **h**, Overlay of the two images in **g**. Detailed image acquisition and analysis parameters are provided in Supplementary Table 1, and colour maps for ultrasound images in Supplementary Fig. 9. The size of each field of view is indicated in the lower right corner of the images. All error bars represent \pm s.e.m.

Ana gas vesicle well and the mixed well is also eliminated, leaving only background (Fig. 2f, bottom). *Halo* gas vesicle contrast can now be inferred by subtracting the second image from the first image (Fig. 2g, top) and *Ana* gas vesicle contrast can be calculated by subtracting the third image from the second image (Fig. 2g, bottom). An overlay correctly shows the mixed well as containing both types of vesicle (Fig. 2h).

Because gas vesicles are smaller than the wavelengths typically used in ultrasound, we further hypothesized that assemblies of gas vesicle nanoparticles would produce enhanced scattering compared to unaggregated solutions, as previously shown with perfluorocarbon droplets¹¹, potentially enabling gas vesicles to serve as biomolecular sensors analogous to aggregation-dependent nanoparticle reporters for magnetic resonance imaging (MRI)²⁰. To test this possibility, we functionalized the surface of *Ana* gas vesicles with biotin and exposed them to various quantities of free streptavidin. In the absence of streptavidin, or at streptavidin concentrations sufficient to saturate surface biotins, the vesicles are expected to remain unaggregated. However, at intermediate concentrations, streptavidin is expected to mediate gas vesicle clustering (Fig. 3a). The formation of aggregates ($\sim 1 \mu\text{m}$) in response to streptavidin was confirmed by transmission electron microscopy (TEM; Fig. 3d) and at higher magnification it was also possible to discern individual streptavidin molecules on the surface of the gas vesicles at the expected relative densities (arrows in Fig. 3d). When nanoparticle assemblies were imaged in ultrasound, the intermediate streptavidin concentration was detected by a twofold increase in contrast (Fig. 3b,c). *Ana* gas

vesicles were chosen for functionalization because their greater resistance to collapse (compared to *Halo* vesicles) allows easier handling during repeated purifications.

Next, to test the feasibility of using gas vesicles expressed inside cells as intracellular reporters or genetic labels, we imaged intact *Ana* cells and compared the resulting contrast to vesicles that were released from the same quantity of cells through hypertonic lysis (Fig. 3e–g). The intact cells exhibited a 12-fold stronger signal, indicating that intracellular gas vesicles have the potential to serve as genetically encoded reporters or dynamic indicators of cellular integrity. The quantity of gas vesicles recovered after lysis ($815 \pm 124 \mu\text{l}$ gas volume per gram of dry cell pellet, $N = 4$) was greater than previously measured intracellular gas vesicle contents (~ 350 – $500 \mu\text{l g}^{-1}$)^{21,22}, suggesting that the observed difference in contrast between intact and lysed cells is unlikely to arise from vesicle destruction during lysis.

Finally, to demonstrate that gas vesicles are capable of producing ultrasound contrast *in vivo*, we performed subcutaneous and intra-venous injections of *Halo* gas vesicles into live anaesthetized mice, choosing *Halo* vesicles for their robust nonlinear signals (Fig. 2a). We first injected the gas vesicles or a buffer control subcutaneously into the lower abdomen of anaesthetized CD-1 mice and acquired second-harmonic images (transmitting at 6 MHz) using our single-element apparatus. We observed robust enhancement on the gas vesicle side (Fig. 4a,b,d), but not on the control side. To confirm that the vesicles were the source of the observed contrast, we applied ultrasonic pulses at a supravascular pressure (650 kPa),

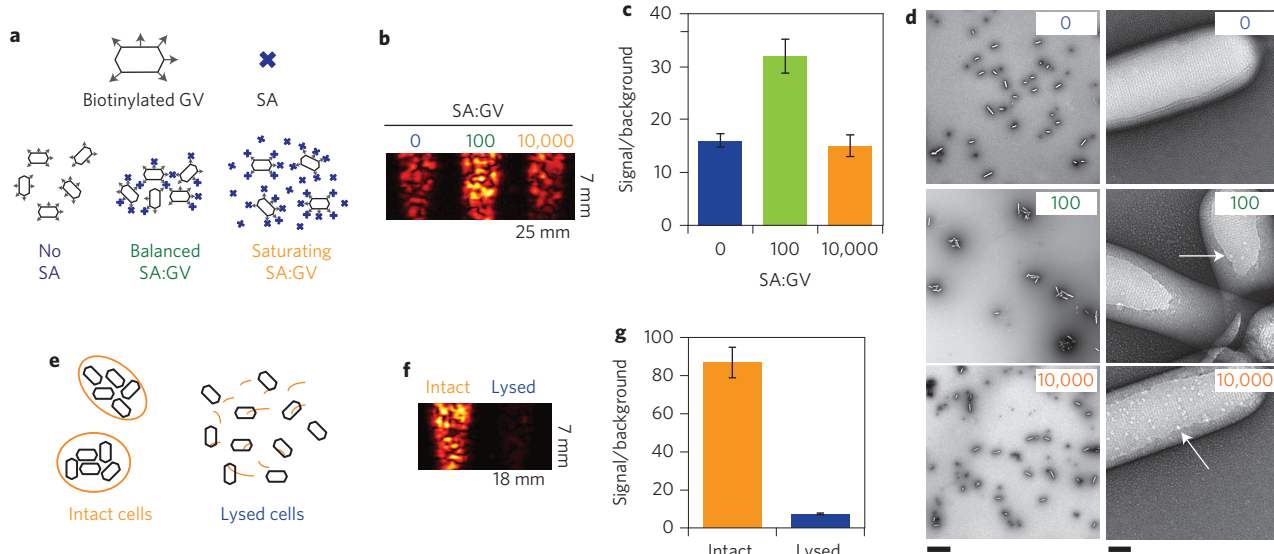


Figure 3 | Gas vesicles act as biomolecular sensors and report cellular integrity. **a**, Illustration of predicted aggregation interactions between surface-biotinylated gas vesicles (hexagons with grey arrows) and streptavidin (SA) at different SA:GV ratios. **b**, An image, acquired at 17 MHz, of OD 1.0 biotinylated *Ana* gas vesicles mixed with the indicated ratio of streptavidin. **c**, Integrated signal intensity relative to phantom background corresponding to the SA:GV conditions in **b** ($N = 4$ per condition). **d**, TEM images of *Ana* gas vesicles incubated with streptavidin at the indicated molar ratios on the top right-hand corner of each panel. At the higher magnification (right), arrows indicate apparent streptavidin molecules on the vesicle surface. Scale bars, 2 μm (left) and 40 nm (right). **e**, Illustration of gas vesicles (black hexagons) confined inside intact cells (orange) or released following lysis. **f**, Ultrasound image (17 MHz pulses) of *Ana* cells treated with water (intact) or with 25% sucrose (lysed). **g**, Integrated signal intensity relative to phantom background for intact and lysed cells ($N = 4$ per condition). Detailed image acquisition and analysis parameters are provided in Supplementary Table 1, and colour bars for ultrasound images in Supplementary Fig. 9. The size of each field of view is indicated in the lower right corner of the images. All error bars represent \pm s.e.m.

resulting in contrast disappearance (Fig. 4c,d). Regions of interest containing gas vesicles exhibited $60 \pm 14\%$ stronger backscattered signals than buffer-injected controls ($P = 0.008$); this difference disappeared after collapse ($P = 0.23$). Images from five animals are shown in Supplementary Fig. 4. In addition, we used a commercial high-frequency small-animal ultrasound scanner operating at 18 MHz to image the dynamics of *Halo* gas vesicles (50 μl , OD 6.0) injected into the tail vein of severe-combined immunodeficient (SCID) nude mice. Five seconds after the start of the injection (at a rate of 0.6 ml min^{-1}), robust scattering was observed from the inferior vena cava (IVC) in nonlinear contrast images (Fig. 4e,h,i and Supplementary Movie 1). Then, as expected for unfunctionalized nanostructures, gas vesicle contrast accumulated in the liver, reaching a steady state after ~ 50 s (Fig. 4f,h,j and Supplementary Movie 1). Application of a high-power burst from the transducer completely eliminated the accumulated contrast (Fig. 4g,h,i,j and Supplementary Movie 1). Under these conditions, gas vesicles were detectable *in vivo* when injected at concentrations as low as OD 1.5 in the IVC (Fig. 4k), and OD 3.0 in the liver (Fig. 4l); contrast increased with dosing above these levels.

No acute toxicity was observed in the intravenously injected mice. The animals' heart rates and breathing remained normal during and after imaging (Supplementary Fig. 5), and no significant decrease in five veterinary health measures (activity, weight, food intake, posture and hydration) was observed immediately or 24 and 48 h after vesicle administration (Supplementary Table 2). Gas vesicles taken up by the liver appeared to be degraded within 60 min of uptake (Supplementary Fig. 6), consistent with other protein nanostructures cleared by this organ, such as bacteriophage²³. However, when vesicles were injected subcutaneously, occupying a tissue that lacks rapid nanoparticle clearance and protein degradation, they produced stable contrast for at least 2 h (Supplementary Fig. 7).

Our findings establish gas vesicles as a promising new class of molecular reporters for ultrasonography. Their ability to produce stable

contrast at subnanomolar reporter concentrations may enable future applications of ultrasound in imaging studies that, to date, have been dominated by nanoparticle reporters for other modalities such as MRI and fluorescence¹⁴. These concentrations represent gas contents ($<1 \mu\text{l gas/ml solution}$) similar to those of typical formulations of microbubbles, which contain $\sim 1,000$ times more gas per particle¹⁹. Furthermore, several of the demonstrated acoustic properties, including response at high frequencies (up to the measured 18 MHz), ability to produce harmonic signals (in *Halo* gas vesicles) and controlled acoustic collapsibility *in situ*, are especially advantageous for high-resolution contrast-enhanced imaging²⁴. Future work is needed to determine how these properties are influenced by the specific size, shape, elasticity, gas diffusivity and collapse-resistance of these nanostructures. Some insights may be gained by refining existing microbubble theories, which predict peak responses at frequencies >18 MHz for contrast agents with submicrometre size and relatively high stiffness^{18,25–27}. In addition, differences in the physical properties of gas vesicles obtained from distinct species, such as sharply tuned collapse pressures and harmonic scattering, may enable new detection schemes, as shown here with serial collapse imaging of gas vesicles from *Ana* and *Halo*.

Application-specific reporters can be generated by functionalizing the surface of gas vesicles through bioconjugation, as shown here with clustering-based analyte (streptavidin) detection by biotinylated *Ana* gas vesicles. The nanometre dimensions of these structures may enable the labelling of targets outside the bloodstream, such as tumours with increased vascular permeability²⁸, to be explored in future studies. As with other nanoscale imaging agents, PEGylation or other surface treatments may be necessary to increase circulation time, reduce clearance by organs such as the liver, and decrease immunogenicity²⁹. Future work is also needed to demonstrate the safety of gas vesicles for potential clinical and preclinical applications, including those that may require repeated administration.

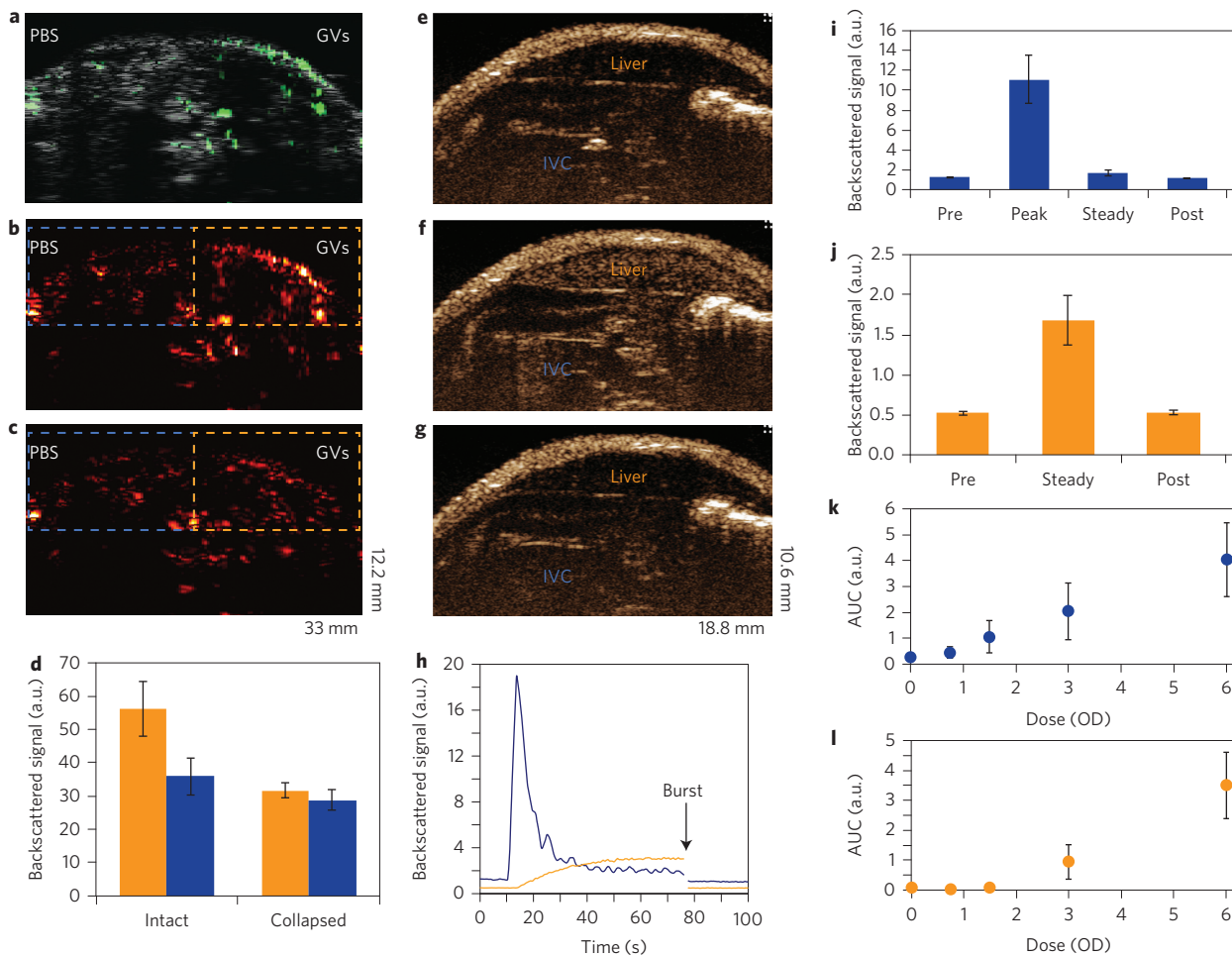


Figure 4 | Gas vesicles produce ultrasound contrast *in vivo*. **a**, Overlay of second-harmonic image (6 MHz pulses) in green on a greyscale broadband anatomical image of mouse lower abdomen injected subcutaneously with 150 μ l OD 6.0 *Halo* gas vesicles on the right side and 150 μ l PBS on the left side. **b,c**, Second-harmonic ultrasound images before (**b**) and after (**c**) vesicle collapse with destructive insolation (650 kPa). Dashed outlines show regions of interest (ROI) used to quantify signals. **d**, Total backscattered second harmonic signal from ROIs covering vesicle-injected (orange) and PBS-injected (blue) tissues, before and after collapse ($N = 5$). **e–g**, Nonlinear contrast images acquired using a high-frequency ultrasound scanner system (operating at 18 MHz and 2% power) of SCID nude mice infused intravenously with 50 μ l OD 6.0 *Halo* gas vesicles. The images show contrast at 4.5 s (**e**) and 64 s (**f**) after the start of infusion, or after the application of a burst pulse (**g**). Locations of the IVC and liver are indicated. **h**, Time course of the smoothed average nonlinear signal in the IVC (blue) and liver (orange) during infusion. **i**, Mean average signal intensity in the IVC before (pre), during (peak) and after (steady) infusion, and after the burst pulse (post) ($N = 5$). **j**, Mean average signal intensity in the liver before (pre) and after (steady) infusion, and after the burst pulse (post) ($N = 5$). **k,l**, Dose-response relationship of 50 μ l *Halo* gas vesicles infused at OD 0–6.0 determined from the AUC of average contrast in the IVC (**k**) and liver (**l**) ($N = 5$). Detailed image acquisition and analysis parameters are provided in Supplementary Table 1, and colour maps for ultrasound images in Supplementary Fig. 9. The size of each field of view is indicated in the lower right corner of the images. All error bars represent \pm s.e.m.

Intriguingly, the intracellular detectability of gas vesicles suggests that they could, in the future, be developed as reporter genes for bacterial or mammalian cell tracking, potentially enabling longer-term monitoring than recently demonstrated with microbubbles⁸. Indeed, gene clusters encoding gas vesicles have already been heterologously expressed in *Escherichia coli*³⁰. Furthermore, genetic sequence control over the size, shape and collapse pressures of gas vesicles in their native hosts³ could assist with the optimization of gas vesicle properties for future use as either injectable or encoded reporters.

Finally, we note that the well-defined molecular structures, anisotropic shapes, hollow interiors, gas permeability, optical scattering, buoyancy, chemical reactivity, controlled collapse and genetic encoding of gas vesicles could conceivably make them useful in various other nanotechnology applications.

Methods

For additional details see Supplementary Information.

Gas vesicle preparation. *Anabaena flos-aquae* (*Ana*) was cultured in Gorham's media at room temperature under office fluorescent lighting. *Halobacterium NRC-1* (*Halo*) was cultured with shaking at 37 °C in ATCC medium 2185, under ambient light. Gas vesicles were isolated from *Ana* and *Halo* using hypertonic and hypotonic lysis, respectively, and purified by repeated centrifugally assisted flotation (Supplementary Fig. 8). Precollapsed gas vesicles were prepared through the application of hydrostatic pressure in a capped syringe.

The concentration of vesicles was estimated based on pressure-sensitive optical density at 500 nm ($OD_{500,PS}$)². The relationship between $OD_{500,PS}$ and protein concentration was determined empirically using a total protein assay. Literature-based estimates of molecular weight^{31–33} were used to calculate molar concentrations. Gas volume fractions were estimated using gas volumes of 8.4 μ l mg⁻¹ and 12.3 μ l mg⁻¹ for *Ana* and *Halo* gas vesicles, respectively^{32,33}.

For experiments comparing intact and lysed cells, *Ana* cultures (cell $OD_{600nm} \approx 2$) were mixed 50:50 with either water or 50% sucrose for 60 min before imaging. Vesicle release was measured using $OD_{500,PS}$ and compared to dry cell pellet weight.

Biofunctionalization and aggregation. *Ana* gas vesicles were biotinylated using sulfo-NHS-LC-biotin and purified by three-times repeated flotation. For aggregation experiments, biotinylated vesicles were mixed with streptavidin at indicated molar ratios for \sim 30 min before imaging.

In vitro ultrasound imaging. Imaging phantoms were prepared from 1% agarose in water. Two times concentrated gas vesicle samples were mixed 1:1 with melted 1% agarose, and 100 µl of the mixture was quickly loaded into phantom wells. The same procedure was used to load polystyrene microspheres (0.83% final wt/vol, 4.78 µm). Imaging was performed using a home-built imaging set-up. A 5, 10 or 20 MHz single-element transducer (6.3, 6.3 and 3.2 mm active areas, respectively; 25.4 mm focal distance) was mounted on a computer-controlled two-dimensional translating stage, immersed in water ~20 mm above the sample. A programmable pulse generator and radiofrequency amplifier drove the transducers at specified frequencies with sinusoidal pulse trains of ~1 µs. The preamplifier function of a pulse receiver with high-pass and low-pass filtering at 5 MHz and 75 MHz, connected to an oscilloscope, was used to collect ultrasound signals and record them using MATLAB (Mathworks). *In situ* vesicle collapse was obtained by repeated pulsing at the indicated pressures at 8 or 8.6 MHz.

Image analysis. MATLAB was used to process raw time-domain data into two-dimensional (B-mode) images. If multiple neighbouring lines perpendicular to the B-mode image were acquired, they were averaged. Regions of interest were defined manually in the axial dimension and automatically in the lateral dimension. Processing and scaling parameters are listed in Supplementary Table 1. Colour maps used in the images are shown in Supplementary Fig. 9. Power spectra represent squared absolute values of fast Fourier transforms of raw time-domain signals.

In vivo imaging. For imaging of subcutaneously injected gas vesicles (Fig. 4a–d) female CD-1 mice under isoflurane anaesthesia were depilated above the lower abdomen and injected subcutaneously with 150 µl *Halo* gas vesicles (OD 6) on one side and 150 µl PBS on the other side of the abdomen. An ultrasonic transducer was coupled through a column of ultrasound gel above the injected region and scanned or used to apply destructive pulses as described above.

Intravenously injected gas vesicles were imaged in SCID nude mice using the VisualSonics Vevo 2100 high-frequency ultrasound scanner operating in nonlinear contrast mode, with the MS250 transducer set to 18 MHz and 2% power. The mice were maintained under isoflurane anaesthesia on a heated imaging platform. Breathing and heart rate were monitored by built-in sensors. During infusion experiments, images were acquired continuously at a frame rate of 15 frames/s for ~100 s. A volume of 50 µl *Halo* gas vesicles in PBS was infused ~10 s after the start of the experiment at a flow rate of 0.6 ml min⁻¹. After 65 s, a burst pulse was applied to collapse the vesicles. ROIs were analysed using Vovo Lab software. Smoothed infusion time-course curves were generated using locally weighted scatterplot smoothing. Area under the curve (AUC) values were obtained from raw data normalized to the pre-infusion baseline. *Halo* gas vesicles remaining in the liver following intravenous injection were imaged as described above, with the additional collection of images during 30 s windows at 15, 30, 45, 60 and/or 75 min after injection. In subcutaneous injection experiments, 100 µl OD 6.0 *Halo* gas vesicles were injected subcutaneously on the right side of the abdomen and 100 µl PBS was injected contralaterally.

Veterinary evaluation. Animals were evaluated by a veterinarian on a 15-point scale comprising three points each for activity, weight, food intake, posture and hydration. The veterinarian was blinded to the injection group.

TEM. TEM images were obtained on a Philips/FEI Tecnai 12 microscope operating at 120 kV. Gas vesicle samples (OD 0.1) were deposited on a carbon-coated formvar grid and stained with 2% uranyl acetate.

Received 20 November 2012; accepted 28 January 2014;
published online 16 March 2014

References

- Smith-Bindman, R. *et al.* Use of diagnostic imaging studies and associated radiation exposure for patients enrolled in large integrated health care systems, 1996–2010. *J. Am. Med. Assoc.* **307**, 2400–2409 (2012).
- Walsby, A. E. Gas vesicles. *Microbiol. Rev.* **58**, 94–144 (1994).
- Pfeifer, F. Distribution, formation and regulation of gas vesicles. *Nature Rev. Microbiol.* **10**, 705–715 (2012).
- Gramiak, R., Shah, P. M. & Kramer, D. H. Ultrasound cardiography—contrast studies in anatomy and function. *Radiology* **92**, 939–948 (1969).
- Ferrara, K., Pollard, R. & Borden, M. Ultrasound microbubble contrast agents: fundamentals and application to gene and drug delivery. *Annu. Rev. Biomed. Eng.* **9**, 415–447 (2007).
- Kaufmann, B. A. & Lindner, J. R. Molecular imaging with targeted contrast ultrasound. *Curr. Opin. Biotechnol.* **18**, 11–16 (2007).
- Cosgrove, D. & Harvey, C. Clinical uses of microbubbles in diagnosis and treatment. *Med. Biol. Eng. Comput.* **47**, 813–826 (2009).
- Cui, W. *et al.* Neural progenitor cells labeling with microbubble contrast agent for ultrasound imaging *in vivo*. *Biomaterials* **34**, 4926–4935 (2013).
- Kircher, M. F., Gambhir, S. S. & Grimm, J. Noninvasive cell-tracking methods. *Nature Rev. Clin. Oncol.* **8**, 677–688 (2011).
- Liu, J. *et al.* Nanoparticles as image enhancing agents for ultrasonography. *Phys. Med. Biol.* **51**, 2179–2189 (2006).

- Lanza, G. M. *et al.* A novel site-targeted ultrasonic contrast agent with broad biomedical application. *Circulation* **94**, 3334–3340 (1996).
- Martinez, H. P. *et al.* Hard shell gas-filled contrast enhancement particles for colour Doppler ultrasound imaging of tumors. *Medchemcomm* **1**, 266–270 (2010).
- Kripfgans, O. D., Fowlkes, J. B., Miller, D. L., Eldevik, O. P. & Carson, P. L. Acoustic droplet vaporization for therapeutic and diagnostic applications. *Ultrasound Med. Biol.* **26**, 1177–1189 (2000).
- James, M. L. & Gambhir, S. S. A molecular imaging primer: modalities, imaging agents, and applications. *Physiol. Rev.* **92**, 897–965 (2012).
- Klebahn, H. Gasvakuolen, ein Bestandteil der Zellen der wasserblutenbildenden Phycochromaceen. *Flora (Jena)* **80**, 241–282 (1895).
- Walsby, A. E. Pressure relationships of gas vacuoles. *Proc. R. Soc. B* **178**, 301–326 (1971).
- Burns, P. N. Harmonic imaging with ultrasound contrast agents. *Clin. Radiol.* **51**, 50–55 (1996).
- De Jong, N., Bouakaz, A. & Frinking, P. Basic acoustic properties of microbubbles. *Echocardiography* **19**, 229–240 (2002).
- Hauff, P., Reinhardt, M. & Foster, S. in *Molecular Imaging I* (eds Semmler, W. & Schwaiger, M.) 223–245 (Springer, 2008).
- Perez, J. M., Josephson, L., O'Loughlin, T., Hogemann, D. & Weissleder, R. Magnetic relaxation switches capable of sensing molecular interactions. *Nature Biotechnol.* **20**, 816–820 (2002).
- Oliver, R. L. & Walsby, A. E. Direct evidence for the role of light-mediated gas vesicle collapse in the buoyancy regulation of *Anabaena flos-aquae* (cyanobacteria). *Limnol. Oceanogr.* **29**, 879–886 (1984).
- Kashyap, S., Sundararajan, A. & Ju, L. K. Flotation characteristics of cyanobacterium *Anabaena flos-aquae* for gas vesicle production. *Biotechnol. Bioeng.* **60**, 636–641 (1998).
- Geier, M. R., Trigg, M. E. & Merril, C. R. Fate of bacteriophage lambda in non-immune germ-free mice. *Nature* **246**, 221–222 (1973).
- Foster, F. S., Pavlin, C. J., Harasiewicz, K. A., Christopher, D. A. & Turnbull, D. H. Advances in ultrasound biomicroscopy. *Ultrasound Med. Biol.* **26**, 1–27 (2000).
- Frinking, P. J. & de Jong, N. Acoustic modeling of shell-encapsulated gas bubbles. *Ultrasound Med. Biol.* **24**, 523–533 (1998).
- Hoff, L., Sontum, P. C. & Hovem, J. M. Oscillations of polymeric microbubbles: effect of the encapsulating shell. *J. Acoust. Soc. Am.* **107**, 2272–2280 (2000).
- Medwin, H. Counting bubbles acoustically: a review. *Ultrasonics* **15**, 7–13 (1977).
- Yuan, F. *et al.* Vascular permeability in a human tumor xenograft: molecular size dependence and cutoff size. *Cancer Res.* **55**, 3752–3756 (1995).
- Jokerst, J. V., Lobovkina, T., Zare, R. N. & Gambhir, S. S. Nanoparticle PEGylation for imaging and therapy. *Nanomedicine* **6**, 715–728 (2011).
- Li, N. & Cannon, M. C. Gas vesicle genes identified in *Bacillus megaterium* and functional expression in *Escherichia coli*. *J. Bacteriol.* **180**, 2450–2458 (1998).
- Jost, M., Jones, D. D. & Weathers, P. J. Counting of gas vacuoles by electron microscopy in lysates and purified fractions of *Microcystis aeruginosa*. *Protoplasma* **73**, 329–335 (1971).
- Walsby, A. E. & Armstrong, R. E. Average thickness of the gas vesicle wall in *Anabaena flos-aquae*. *J. Mol. Biol.* **129**, 279–285 (1979).
- Yao, A. I. & Facciotti, M. T. Regulatory multidimensionality of gas vesicle biogenesis in *Halobacterium salinarum* NRC-1. *Archaea* **2011**, 716456 (2011).

Acknowledgements

The authors thank P. Lum for ultrasound equipment and advice, R. Zalpuri and K. McDonald for assistance with electron microscopy, K.-K. Park and P. Khuri-Yakub for assistance with hydrophone measurements, E. Chérin for input on *in vivo* experiments and the manuscript, and A. Bar-Zion for assistance with data analysis. M.G.S. acknowledges funding from the Miller Research Institute and the Burroughs Wellcome Career Award at the Scientific Interface. Other funding was provided by California Institute for Regenerative Medicine grant RT-02022 (D.V.S.), National Institutes of Health grant R01EB013689 (S.M.C.), the Canadian Institutes of Health Research (F.S.F.) and the Terry Fox Foundation (F.S.F.).

Author contributions

M.G.S. conceived and directed the study, planned the experiments, prepared the specimens, collected, analysed and interpreted the data, and wrote the manuscript, with input from all other authors. P.W.G. designed and constructed the imaging instrument and accompanying signal processing software, and assisted with initial experiments. A.N. designed, constructed and optimized the imaging instrument and accompanying signal processing software. F.S.F. and M.Y. designed, performed and analysed the data from *in vivo* experiments. All authors provided input on the study and experimental design, data analysis, data interpretation and the manuscript.

Additional information

Supplementary information is available in the online version of the paper. Reprints and permissions information is available online at www.nature.com/reprints. Correspondence and requests for materials should be addressed to M.G.S.

Competing financial interests

F. Stuart Foster is a consultant to VisualSonics.

Biogenic gas nanostructures as ultrasonic molecular reporters

Mikhail G. Shapiro*, Patrick W. Goodwill, Arkosnato Neogy, Melissa Yin, F. Stuart Foster, David V. Schaffer, Steven M. Conolly

CONTENTS

1. Supplementary Detailed Methods
2. Supplementary Table S1 – Imaging parameters
3. Supplementary Table S2 – Gas vesicle toxicity assessment
4. Supplementary Figure S1 – Gas vesicle longevity
5. Supplementary Figure S2 – Attenuation effect from *Halo* gas vesicles
6. Supplementary Figure S3 – Harmonic response of *Ana* gas vesicles
7. Supplementary Figure S4 – Gas vesicle imaging *in vivo*
8. Supplementary Figure S5 – Effect of gas vesicle injection on heart rate and breathing
9. Supplementary Figure S6 – Gas vesicle clearance in the liver
10. Supplementary Figure S7 – Persistent gas vesicle signal after subcutaneous injection
11. Supplementary Figure S8 – Gas vesicle purification from *Ana* and *Halo* cells
12. Supplementary Figure S9 – Colour maps used in ultrasound images
13. Supplementary Figure S10 – Representative regions of interest
14. Supplementary References

Supplementary Detailed Methods

Gas vesicle preparation. *Anabaena flos-aquae* (*Ana*, strain 1403/13F, CCAP, Argyll, Scotland) was cultured in sterile Gorham's media at room temperature under office fluorescent lighting with an approximately 75% circadian duty cycle. *Halobacteria NRC-1* (*Halo*, Carolina Biological Supply, Burlington, NC) was cultured at 37°C in high-salt medium (ATCC medium 2185), under ambient light, with rotation shaking at 225 rpm. GVs were isolated from *Ana* and *Halo* using hypertonic and hypotonic lysis, respectively (for 1 hour at room temperature), and purified by centrifugally-assisted flotation at 300 rcf (Supplementary Fig. S8) Hypertonicity was achieved by adding sucrose to a final concentration of 25%. Hypotonicity was implemented by diluting cells with a >8x volume of low-salt buffer (10mM Tris-HCl, 2.5mM MgCl₂, 0.5mM CaCl₂, pH7.6). To achieve purity (> 6,400X enrichment vs. non-buoyant cellular components), the harvested GVs were twice resuspended in > 80X volumes of phosphate-buffered saline (PBS) and re-centrifugated as above. This procedure is illustrated in Supplementary Fig. 5. GVs were diluted to experimental concentrations using PBS. To prepare pre-collapsed GVs, GV solutions were loaded into capped plastic syringes and the plunger depressed until the initially opaque solution (due to light scattering by intact GVs) became translucent (due to absence of light scattering by collapsed GVs).

The concentration of GVs was estimated based on their optical density (OD). Solutions of intact GVs appear milky white due to the scattering of light by their gas compartments¹. GV collapse eliminates this light scattering, making it possible to subtract background contributions to the solution OD, yielding the "pressure-sensitive" OD at 500 nm (OD_{500,PS}). The relationship between OD_{500,PS} and protein concentration (in mg/mL) was determined empirically using a total protein assay (micro-BCA kit, Pierce, Rockford, IL) performed on GVs purified as described above. Literature-based estimates of the molecular weight of the GVs (107 MDa for *Ana*, 686 MDa for *Halo*)²⁻⁴ were used to calculate the molar concentration. We obtained a value of 564.2 ± 94.2 pM/ OD_{500,PS} (N=5) and 16.1 ± 3.2 pM/ OD_{500,PS} (N=3) for *Ana* GVs and *Halo* GVs, respectively, which we rounded up to 600 and 20 pM/ OD_{500,PS}, respectively. The value for *Ana* GVs is slightly higher than ~450 pM/ OD_{500,PS} which can be calculated from literature, the discrepancy possibly arising from incomplete GV purity, the presence of popped GVs in the OD measurement and/or differences in the protein assays used. Gas volume fractions were estimated using approximate gas volumes of 8.4 μL per mg and 12.3 μL per mg for *Ana* and *Halo* GVs, respectively, derived from literature^{3,4}.

For experiments comparing intact and lysed cells, concentrated *Ana* cultures (cell OD_{600nm} ~ 2) were mixed 50:50 with either water or 50% sucrose for 60 minutes, then loaded into ultrasound imaging gels as described above. To measure GV release upon lysis, OD_{PS,500} was measured in solutions of lysed cells and compared to the dry pellet weight of paired cell samples (dry pellets were obtained by hydrostatically collapsing GVs inside the cells, pelleting the cells, washing with water, re-pelleting and drying overnight at 80°C).

Bio-functionalization and aggregation. *Ana* GVs were biotinylated using EZ-Link Sulfo-NHS-LC-Biotin (Thermo Scientific, Rockford, IL) following supplier instructions, with a 10,000-fold molar excess of functionalizing reagent per GV, and purified by 3X repeated floatation (as in Supplementary Fig. S5c). For aggregation experiments, biotinylated GVs were mixed with streptavidin (G-Biosciences, St. Louis, MO) at indicated molar ratios and allowed to react for approximately 30 minutes before imaging.

In vitro ultrasound imaging. Imaging phantoms were prepared by casting 1% agarose gel (in water) around 96-well PCR reaction tubes, which were removed after solidification. 2X concentrated GV samples were mixed 1:1 with melted 1% agarose, and 100μL of the mixture was quickly loaded into phantom wells. The same procedure was used to load polystyrene microspheres (0.83% final w/v, 4.78 μm, SpheroTech, Lake Forest, IL). After all samples have been loaded and solidified, additional 1% agarose was deposited to completely fill the wells and provide a uniform top surface. Imaging was performed using a home-built imaging setup. A 5 MHz, 10 MHz or 20 MHz single element transducer (6.3, 6.3 and 3.2 mm active areas, respectively; 25.4 mm focal distance; Olympus, Waltham, MA) was mounted on a computer-controlled 2D translating stage (VelMex, Bloomfield, NY). Transducer output was calibrated using a hydrophone (HGL-0200, Onda, Sunnyvale, CA). Phantoms were placed in a water container such that transducers could be immersed in the water at a distance of approximately 20 mm above the phantom. A programmable pulse generator (AFG3102, Tektronix, Beaverton, OR) and radio frequency amplifier (BT00500-AlphaS- CW, Tomco, Stepney, Australia) were used to drive transducers at specified frequencies with sinusoidal pulse trains of approximately 1 μs. The pre-amplifier function of a pulse-receiver (Pa-

nametrics/Olympus 5601A/TT) with high-pass and low-pass filtering at 5 MHz and 75 MHz, connected to an oscilloscope (Infiniivision DSOX2004A, Agilent Technologies, Santa Clara, CA; or LeCroy WaveJet 314, Chestnut Ridge, NY) was used to collect ultrasound signals and record them using MATLAB (Mathworks, Natick, MA). *In situ* GV collapse was obtained by repeated pulsing at indicated pressures with a 10 MHz transducer operating at 8 or 8.6MHz. Specific imaging parameters for each figure are listed in Supplementary Table S1.

Image analysis. Image analysis was performed in MATLAB. Raw time-domain signals acquired at each scan point were bandpass-filtered with symmetric Butterworth filters around the transmit or harmonic frequency, as indicated in Supplementary Table S1. After filtering, signals were brought back to baseband and time-gain compensation was applied using an empirically determined exponential coefficient. Line intensity profiles were obtained as the absolute value of a five point convolution of the in-phase and quadrature signal components. The resulting line intensity profiles were placed into arrays to generate two-dimensional B-mode images. The time axis was converted to space using the speed of sound in aqueous media (1540 m/s). If multiple neighboring lines perpendicular to the B-mode image were acquired, they were added together for averaging, as indicated in Supplementary Table S1. The resulting images were auto-scaled for presentation as indicated in Supplementary Table S1. Signals from regions of interest in each image were summated and used to generate quantitative plots. The regions of interest were defined manually in the axial dimension to include the contents of sample wells, and were defined automatically in the lateral dimension by detecting minima in axially integrated line intensity profiles and setting these minima as boundaries separating samples; the fidelity of automatically detected ROIs was always confirmed visually (and found not to require adjustment). Additional processing parameters are listed in Supplementary Table 1. Colour maps used in the images are shown in Supplementary Fig. S9. Power spectra represent squared absolute values of fast Fourier transforms of raw time-domain signals from regions of interest corresponding to wells containing GVs or polystyrene (Fig 2a. is the average of 48 such spectra).

In vivo imaging. All animal protocols were approved by the Animal Care and Use Committee of the University of California at Berkeley and the Animal Care Committee of Sunnybrook Research Institute, as appropriate. For imaging of subcutaneously injected GVs, female CD-1 mice, maintained under isoflurane anesthesia throughout the experiment, were depilated above the lower abdomen and injected subcutaneously with 150 μ L *Halo* GVs (OD 6) on one side and 150 μ L PBS on the other side of the abdomen. Placed on their backs, the mice were fitted with a homemade container allowing a ~3 cm column of ultrasound gel (Aquasonic, Parker Laboratories, Fairfield, NJ) to be placed above the injected region. An abdominal constriction was used to reduce breathing-related motion of the lower abdominal region. An ultrasonic transducer was coupled into the gel and scanned or used to apply destructive pulses as described above. To image animal anatomy (e.g., Fig. 4a), the pulse generation function of the pulse-receiver was used in place of the signal generator/amplifier. Additional scan parameters are listed in Supplementary Table S1.

Intravenously injected GVs were imaged in SCID nude mice using the VisualSonics Vevo 2100 high frequency ultrasound scanner operating in non-linear contrast mode, with the MS250 transducer set to 18 MHz and 2% power. The mice were maintained under isoflurane anesthesia and placed in supine position on a heated imaging platform. Breathing and heart rate were monitored by built-in sensors. The transducer was positioned above the abdomen such that the field of view would include the liver and the inferior vena cava. During infusion experiments, images were acquired continuously at a frame rate of 15frames/sec for approximately 100 seconds. 50 μ L of *Halo* GVs in PBS at the indicated concentrations were infused approximately 10 seconds after the start of the experiment at a flow rate of 0.6 mL/min. After 65 seconds, a burst pulse (100% power) was applied for 1 second to collapse the GVs. To quantify contrast, ROIs encompassing the inferior vena cava and liver were drawn manually in the Vevo Lab software (for example, see Supplementary Fig. S10), and the averaged non-linear contrast signal within each ROI for each frame was exported into MATLAB for further analysis. Smoothed infusion time course curves were generated from the raw signal using a locally weighted scatterplot smoothing algorithm⁵, which was further used to obtain pre-infusion, peak, steady state, and post-burst intensity values. To obtain AUC values, raw data was normalized to the average pre-infusion baseline, and positive signal values preceding the burst pulse were summated.

Halo GVs remaining in the liver following intravenous injection were imaged as described in the preceding paragraph, with the additional collection of images during 30-second windows at 15, 30, 45, 60

and optionally 75 minutes after injection. The liver signal in each image was quantified using ROI analysis as described above.

To image the persistence of *Halo* GV contrast after subcutaneous injection, 100 µL OD 6.0 *Halo* GVs were injected subcutaneously on the right side of the abdomen of a SCID nude mouse and 100 µL PBS was injected subcutaneously on the left side. The mouse was imaged using the Vevo 2100 system as described above. Images were collected immediately after injection and every 15 minutes thereafter for 120 minutes. A high-pressure burst pulse was applied to collapse any GVs still present after 120 minutes and imaged again.

Veterinary evaluation. The health of animals injected intravenously with OD 6.0 *Halo* GVs or PBS was evaluated by a veterinarian at Sunnybrook Research Institute on a 15-point scale comprising three points each for activity, weight, food intake, posture and hydration. The veterinarian was blinded to the injection group.

Transmission electron microscopy (TEM). TEM images were obtained on a Philips/FEI (Hillsboro, OR) Tecnai 12 microscope operating at 120kV. 10X diluted GV samples (from starting OD 1.0) were deposited on a carbon-coated formvar grid and negatively stained with 2% uranyl acetate in preparation for TEM imaging.

Supplementary Table S1 – Image Acquisition and Analysis Parameters

| Figure | Transmit Frequency | Pulse Source | Peak Pressure | Pulse Train (us) | Averages / line | Perpendicular averages (distance) | Analysis Center Frequency | Analysis Bandwidth | Color map | Color map max | Color map min |
|-----------------------------|--------------------|--------------|-----------------|------------------|-----------------|-----------------------------------|---------------------------|--------------------|----------------|----------------------------|---------------|
| 1d – top | 17Mhz | SG | 175kPa | 1µs | 512 | 3 (1mm) | 17MHz | 4MHz | Hot | 40X STD of PBS well | 0 |
| 1d – middle | 8.6Mhz | SG | 189kPa | 1µs | 512 | 3 (1mm) | 8.6MHz | 4MHz | Hot | 10X STD of PBS well | 0 |
| 1d – bottom | 4.8Mhz | SG | 148kPa | 1µs | 512 | 3 (1mm) | 4.8MHz | 4MHz | Hot | 10X STD of PBS well | 0 |
| 1e - top | 17Mhz | SG | 175kPa | 1µs | 512 | 3 (1mm) | 17MHz | 4MHz | Hot | 40X STD of PBS well | 0 |
| 1e- middle | 8.6Mhz | SG | 189kPa | 1µs | 512 | 3 (1mm) | 8.6MHz | 4MHz | Hot | 10X STD of PBS well | 0 |
| 1e - bottom | 4.8Mhz | SG | 148kPa | 1µs | 512 | 3 (1mm) | 4.8MHz | 4MHz | Hot | 10X STD of PBS well | 0 |
| 2b - top | 6MHz | SG | 98kPa | 1µs | 512 | 3 (1mm) | 6MHz | 4MHz | Hot | 0.7X MI | 0 |
| 2b - middle | 6MHz | SG | 98kPa | 1µs | 512 | 3 (1mm) | 12MHz | 4MHz | Hot | MI | 0 |
| 2b - bottom | 6MHz | SG | 98kPa | 1µs | 512 | 3 (1mm) | 18MHz | 4MHz | Hot | MI | 0 |
| 2d - top | 8.6MHz | SG | 166kPa | 1µs | 512 | 3 (1mm) | 8.6MHz | 4MHz | Hot | 0.7X MI | 0 |
| 2d - middle | 8.6MHz | SG | 166kPa | 1µs | 512 | 3 (1mm) | 8.6MHz | 4MHz | Hot | 0.7X MI of 2d top | 0 |
| 2d - bottom | Calculated | | | | | | | | Hot | 0.7X MI of 2d top | 0 |
| 2f | 8.6MHz | SG | 166kPa | 1µs | 512 | 3 (1mm) | 8.6MHz | 4MHz | Hot | 0.5 MI | 0 |
| 2g,h-magenta | | | | | | | | | Magenta | 0.8X MI | 0 |
| 2g,h - green | | | | | | | | | Green | 0.4X MI | 0 |
| 3b | 17MHz | SG | 77kPa | 1µs | 64 | 1 | 17MHz | 4MHz | Hot | MI | 0 |
| 3f | 17MHz | SG | 77kPa | 1µs | 64 | 1 | 17MHz | 4MHz | Hot | MI | 0 |
| 4a - gray | 10MHz transducer | PR | Power setting 4 | n/a | 512 | 3 (0.1mm) | 10MHz | 10MHz | Gray | 0.2X MI | 0 |
| 4a - green | 6MHz | SG | 85kPa | 1µs | 512 | 3 (0.1mm) | 12MHz | 4MHz | Black to green | 0.35X MI | 0.14X MI |
| 4b, c | 6MHz | SG | 85kPa | 1µs | 512 | 3 (0.1mm) | 12MHz | 4MHz | Hot | 0.7X MI | 0.035 X MI |
| 4e-i | 18MHz | Vevo | 2% power | n/a | n/a | n/a | Contrast mode | n/a | Vevo std. | Vevo std. | Vevo std. |
| Sup. S1 | 17Mhz | SG | 175kPa | 1µs | 512 | 3 (1mm) | 17MHz | 4MHz | Hot | 100X avg. intensity of PBS | 0 |
| Sup. S2 | 17MHz | SG | 175kPa | 1µs | 512 | 3 (1mm) | 17MHz | 4MHz | Hot | Scaled to show shadowing | 0 |
| Sup. S4 a, d, g, j, m | 10MHz transducer | PR | Power setting 4 | n/a | 512 | 3 (0.1mm) | 10MHz | 10MHz | Gray | 0.2X MI | 0 |
| Sup. S4 b,c,e,f, k, l, n, o | 6MHz | SG | 85kPa | 1µs | 512 | 3 (0.1mm) | 12MHz | 4MHz | Hot | 0.7X MI | 0.035 X MI |
| Sup. S4 h, i | 6MHz | SG | 85kPa | 1µs | 512 | 3 (0.1mm) | 12MHz | 4MHz | Hot | 0.5X MI | 0.025 X MI |

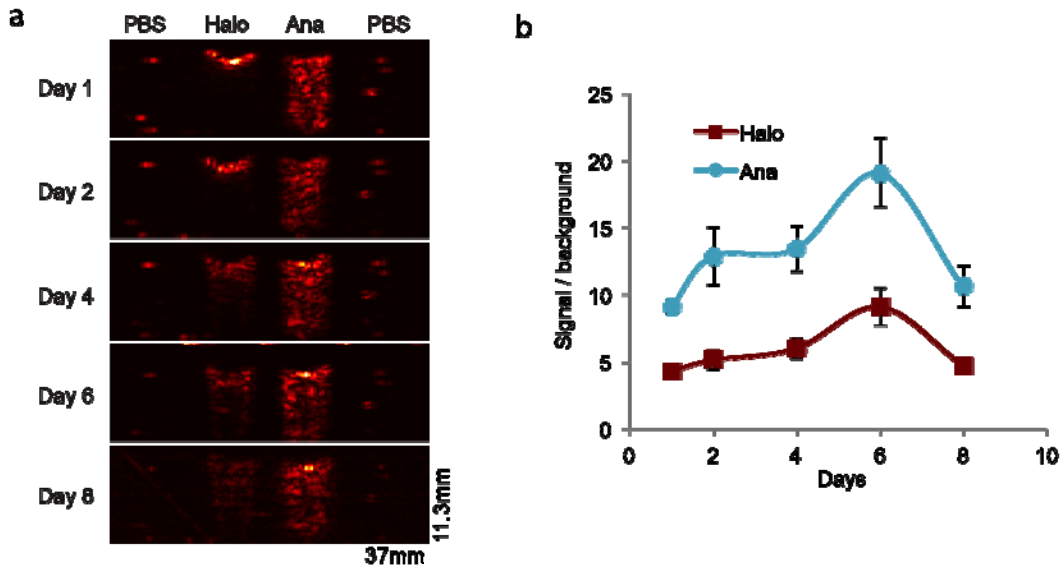
Abbreviations: SG – Signal generator, PR – Pulse receiver, Vevo – Vevo 2100 ultrasound scanner; STD – Standard deviation, MI – Maximum intensity

Supplementary Table S2 – Gas Vesicle Toxicity Assessment

| | GVs | Saline |
|-------------|------------|---------------|
| Pre | 15 | 15 |
| Post | 15 | 15 |
| 24h | 14.7±0.3 | 15 |
| 48h | 15 | 15 |

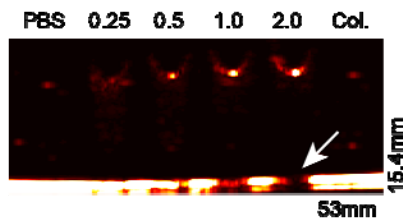
Supplementary Table S2 - Gas vesicle toxicity assessment. Mean health grades of mice injected intravenously with 50µL OD 6.0 *Halo* GV_s or PBS. Mice were scored on a 15-point scale comprising 3 points each for activity, weight, food intake, posture and hydration by a veterinarian blinded to injection group. Evaluations were performed before, immediately after and 24 and 48 hours after injection. (N=3, ±SEM). Only one mouse (at 24h) scored less than 15 points due to a minor drop in weight (resulting in a 14/15 score), and recovered by 48h.

Supplementary Figure S1



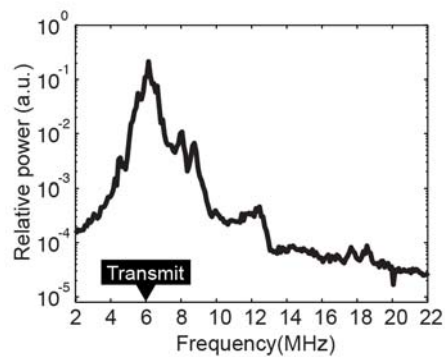
Supplementary Figure S1. Gas vesicle longevity. **a**, Ultrasound image (17 MHz pulses) of a phantom containing PBS buffer, OD 2.0 *Halo* GVs, OD 2.0 *Ana* GVs or another well of PBS buffer, acquired repeatedly over several days, as indicated. Note that the intensity profile of *Ana* GVs shows minimal change. *Halo* GV signal appears to show less of a shadowing effect, potentially indicative of a decrease in *Halo* GV concentration. **b**, Total backscattered signal from *Halo* and *Ana* GVs on each day of sampling, relative to PBS controls (N=4/sample). Detailed image acquisition and analysis parameters are provided in Supplementary Table S1; colour map in Supplementary Fig. S6. Error bars represent \pm SEM. The size of the field of view is indicated in the lower right corner of the bottom image.

Supplementary Figure S2



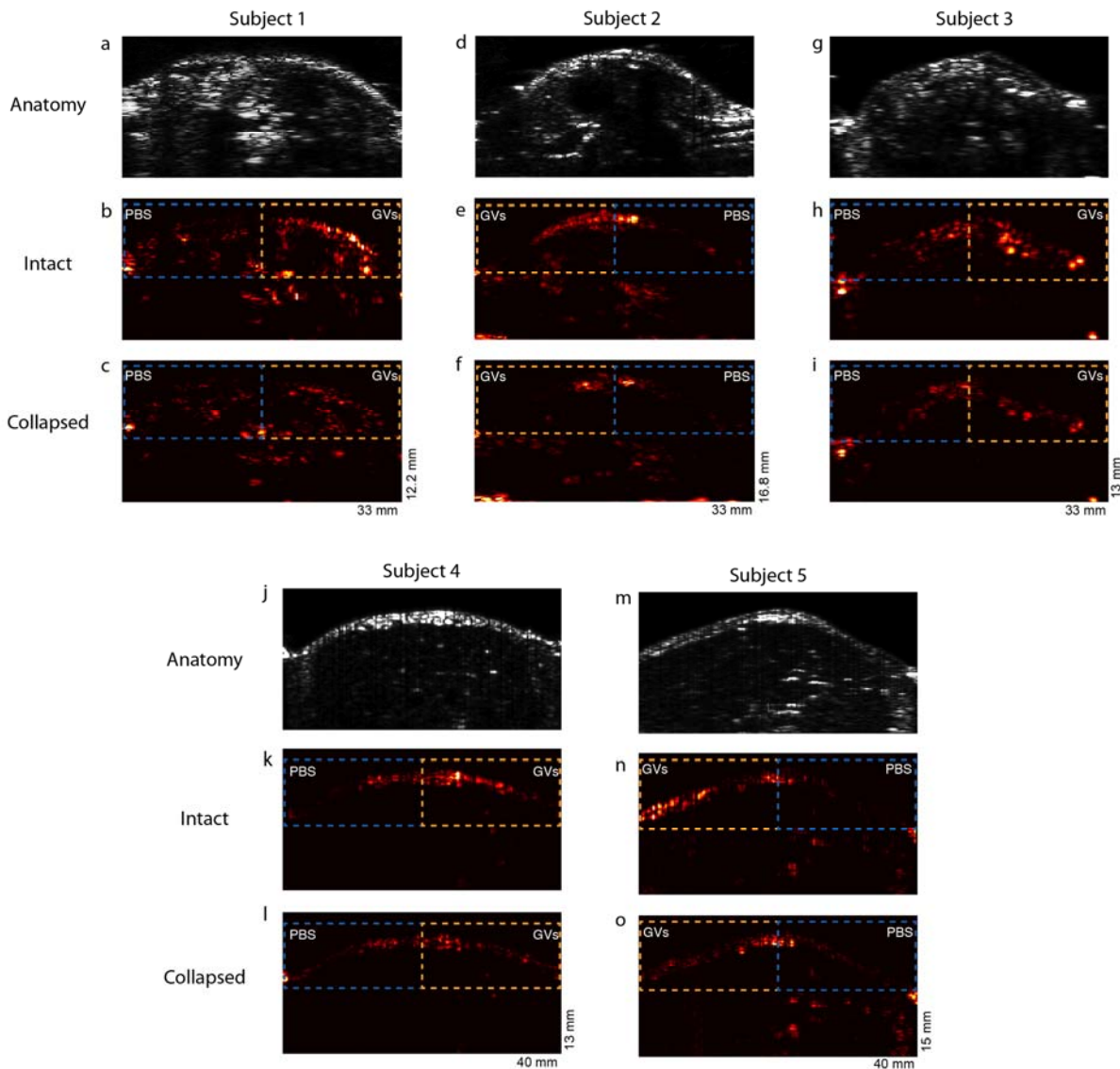
Supplementary Figure S2. Attenuation effect from *Halo* gas vesicles. Ultrasound image (17MHz) of phantom containing PBS buffer, *Halo* GVs at indicated optical densities or collapsed OD 2.0 *Halo* GVs. The intense signal at the bottom of the image corresponds to the solid bottom of the imaging phantom. The arrow points to a location underneath *Halo* GVs where the signal from the solid bottom is attenuated. Smaller attenuation can be observed at lower concentrations of GVs. Detailed image acquisition and analysis parameters are provided in Supplementary Table S1; colour map in Supplementary Fig. S6. The size of the field of view is indicated in the lower right corner of the bottom image.

Supplementary Figure S3



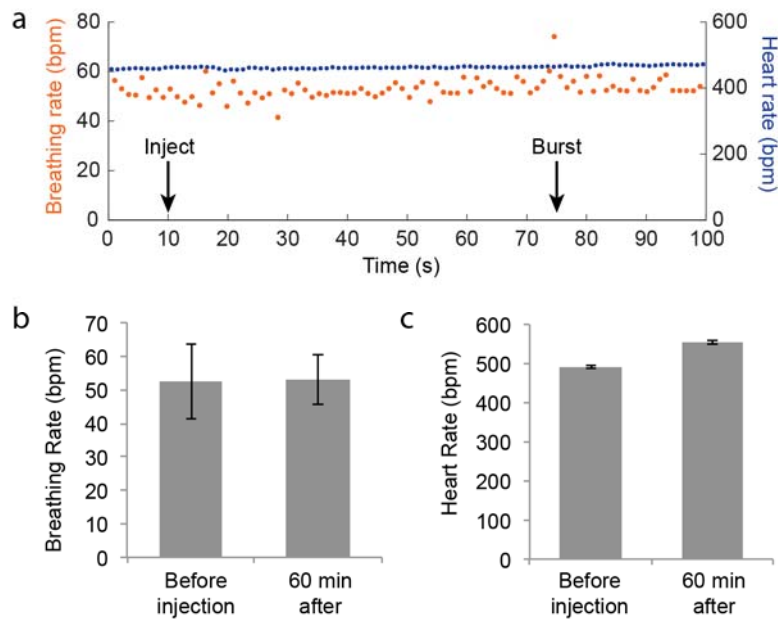
Supplementary Figure S3. Harmonic ultrasound response of *Ana* GVs. Power spectrum of signal backscattered from OD 2.0 *Ana* GVs in response to 6 MHz ultrasound pulses (peak amplitude 98 kPa). Each point represents an average of 16 measurements.

Supplementary Figure S4



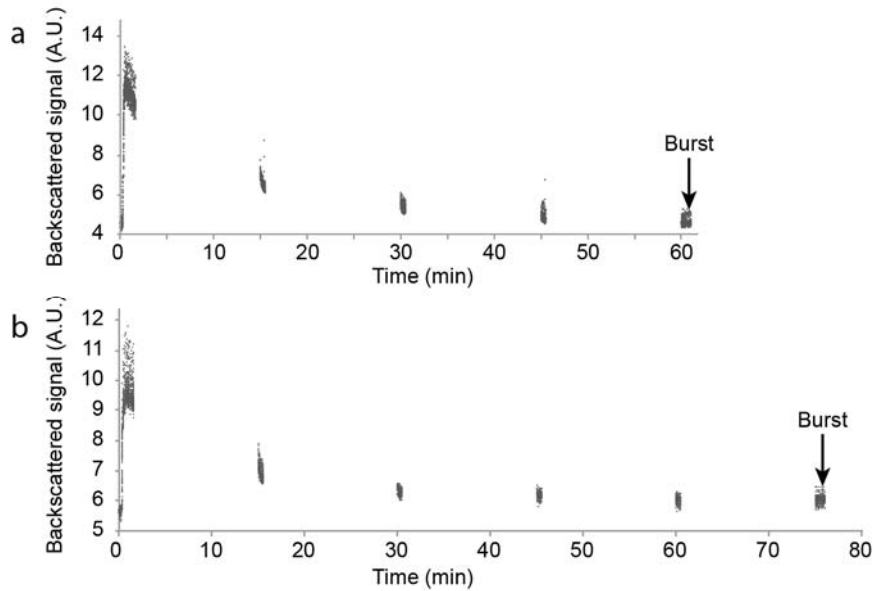
Supplementary Figure S4. Gas vesicle imaging *in vivo*. **a**, Three mice were depilated and injected subcutaneously with 150 μ L OD 6.0 *Halo* GVs or 150 μ L PBS on opposite sides of the abdomen, as indicated. **a, d, g, j, m**, Anatomical ultrasound images acquired with 10MHz transducer. **b, e, h, k, n**, 12MHz harmonic ultrasound images (6MHz pulsing). **c, f, i, l, o**, 12MHz harmonic ultrasound images after GV collapse with destructive insonation. Dashed ovals indicate approximate location of injected material. Subject 1 is also shown in Figure 4. Detailed image acquisition and analysis parameters are provided in Supplementary Table S1; colour maps in Supplementary Fig. S6. The size of the field of view is indicated in the lower right corner of the bottom image.

Supplementary Figure S5



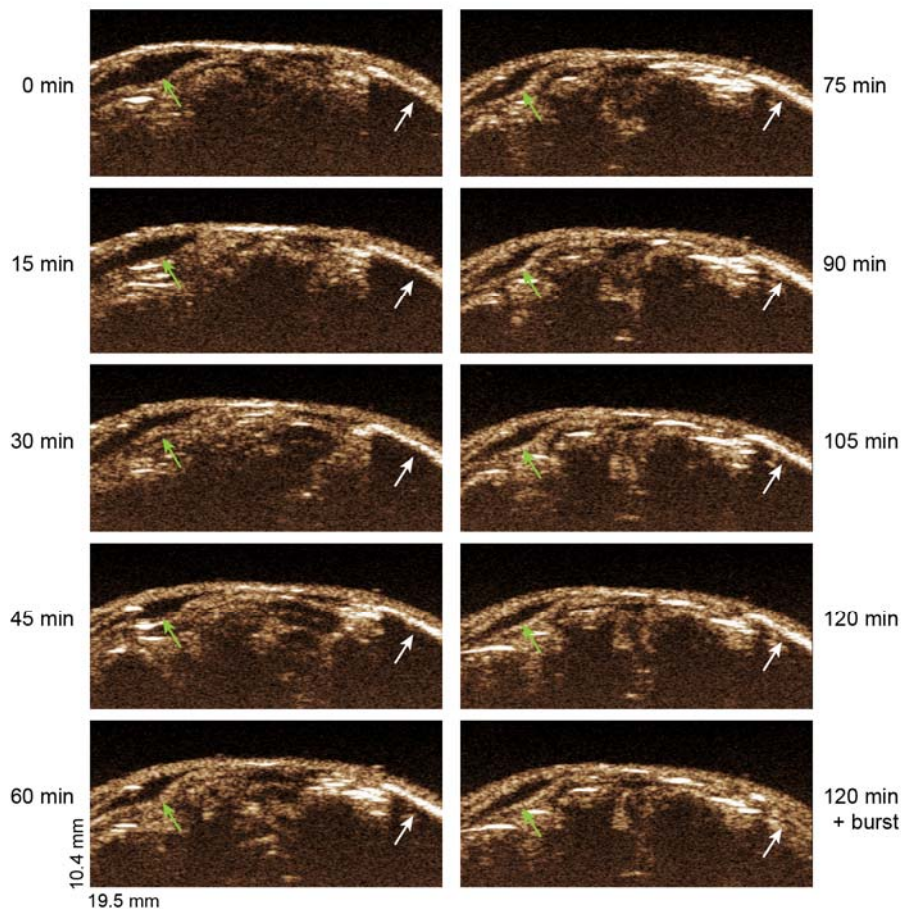
Supplementary Figure S5. Effect of gas vesicle injection on heart rate and breathing. **a.** Heart rate and breathing rate recorded during a *Halo* GV injection such as the one shown in Fig. 4, h. Arrows indicate the approximate timing of GV injection and the burst pulse. **b-c.** Mean heart rate (b) and breathing rate (c) measured immediately before and 60 min after intravenous injection of 50 μ L OD 6.0 *Halo* GVs. N=4. Error bars \pm SEM.

Supplementary Figure S6



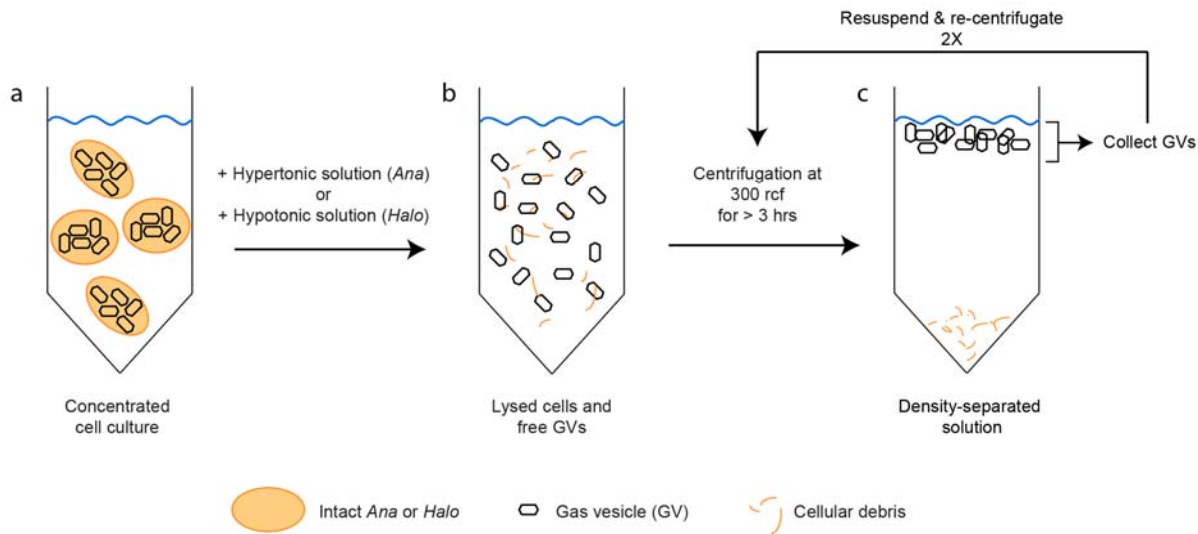
Supplementary Figure S6. Gas vesicle clearance in the liver. Backscattered non-linear signal in the livers of two mice (shown in **a** and **b**) injected intravenously with OD 6.0 *Halo* GVs. Injection, imaging parameters and ROI analysis were the same as for Fig 4, e-h, except that mice were kept anesthetized for 60-80 minutes after injection with imaging repeated every 15 minutes, as shown. At either 60 (a) or 75 (b) minutes after injection, a high-pressure burst pulse was applied to collapse any remaining GVs (as indicated by arrows).

Supplementary Figure S7



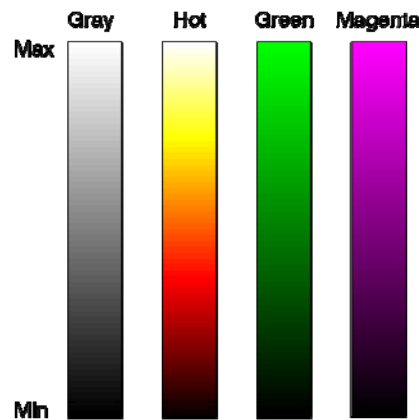
Supplementary Figure S7. Persistent gas vesicle signal after subcutaneous injection. Non-linear contrast images of SCID nude mice injected subcutaneously with 100 μ L OD 6.0 *Halo* GVs (right side) or 100 μ L PBS buffer (left side), acquired using a high-frequency ultrasound scanner system operating at 18 MHz and 2% power. The images were taken immediately after injection and every 15 minutes thereafter as indicated next to each image. A high-pressure burst pulse was applied to collapse the GVs still present after 120 minutes, resulting in the bottom right image. The white arrow denotes contrast attributed to GVs (and its absence after the burst pulse). Note that the GVs show up as a bright anterior line of robust echogenicity with strong shadowing of the distal tissue below it due to attenuation (consistent with Supplementary Fig. S2). Brightening of the GV signal during the first hour of imaging is attributed to absorption of the PBS fluid in which the GVs are injected, increasing their local concentration; absorption of the fluid pocket is also observed on the control side. Both the highly echogenic signal and the shadowing are eliminated by the burst after 120 min. The green arrow indicates the expected location of the injected PBS.

Supplementary Figure S8



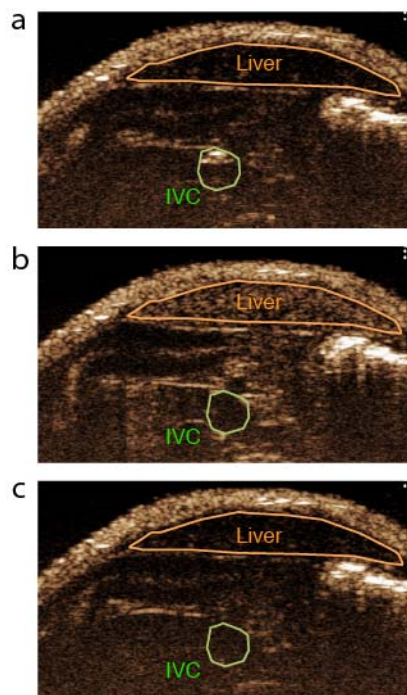
Supplementary Figure S8. Gas vesicle purification from *Ana* and *Halo* cells. GVs are purified through tonic lysis of cells followed by centrifugally-assisted floatation. **a.** Concentrated suspensions of *Ana* or *Halo* cells are disrupted through hypertonic lysis (addition of 25% sucrose) or hypotonic lysis (8-fold dilution in low-osmolarity buffer), respectively, for 1 hour. **b.** The resulting suspension is centrifugated for 3 hours or longer at 300 rcf (this low speed is chosen to prevent GV disruption by pressure). **c.** GVs are collected from the surface of the centrifugated solution, re-suspended in > 80X PBS and re-centrifugated. This step is repeated twice.

Supplementary Figure S9



Supplementary Figure S9. Colour maps used in ultrasound images. Gray, Hot, Green and Magenta colour maps as used in Figs. 1-4 in the main text and Supplementary Figs. S1, S2 and S4. The scales are linear between Min and Max. The colour map used and the values of Min and Max are defined for each image in Supplementary Table S1. The colour maps Gray and Hot are standard in MATLAB. Green and Magenta were prepared by replacing the color white with either green or magenta in the Gray color map.

Supplementary Figure S10



Supplementary Figure S10. Representative regions of interest used to generate Fig. 4, h-l. Non-linear contrast images showing representative regions of interest (ROIs) for the liver and inferior vena cava (IVC), which were used to generate the data shown in Fig. 4, h-l.

Supplementary References

1. Walsby, A.E. Gas vesicles. *Microbiol. Rev.* **58**, 94-144 (1994).
2. Jost, M., Jones, D.D. & Weathers, P.J. Counting of gas vacuoles by electron microscopy in lysates and purified fractions of *microcystis aeruginosa*. *Protoplasma*, 329-335 (1971).
3. Walsby, A.E. & Armstrong, R.E. Average thickness of the gas vesicle wall in *Anabaena flos-aquae*. *J. Mol. Biol.* **129**, 279-285 (1979).
4. Yao, A.I. & Facciotti, M.T. Regulatory multidimensionality of gas vesicle biogenesis in *Halobacterium salinarum* NRC-1. *Archaea* **2011**, 716456 (2011).
5. Cleveland, W.S. Robust locally weighted regression and smoothing scatterplots. *J. Am. Stat. Assoc.* **74**, 829-836 (1979).